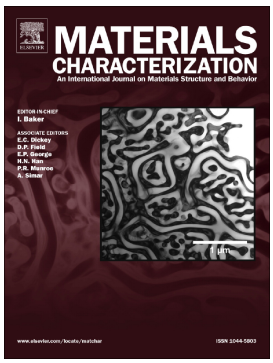
Journal Pre-proof



Strain hardening and strengthening mechanism of laser melting deposition (LMD) additively manufactured FeCoCrNiAl0.5 high-entropy alloy

Lisong Zhu, Keping Geng, Jun Wang, Da Sun, Mengdie Shan, Yao Lu, Xuesong Zhang, Yangchuan Cai, Jian Han, Zhengyi Jiang

PII: S1044-5803(22)00647-7

DOI: https://doi.org/10.1016/j.matchar.2022.112365

Reference: MTL 112365

To appear in: *Materials Characterization*

Received date: 31 July 2022

Revised date: 26 September 2022

Accepted date: 29 September 2022

Please cite this article as: L. Zhu, K. Geng, J. Wang, et al., Strain hardening and strengthening mechanism of laser melting deposition (LMD) additively manufactured FeCoCrNiAl0.5 high-entropy alloy, *Materials Characterization* (2022), https://doi.org/10.1016/j.matchar.2022.112365

This is a PDF file of an article that has undergone enhancements after acceptance, such as the addition of a cover page and metadata, and formatting for readability, but it is not yet the definitive version of record. This version will undergo additional copyediting, typesetting and review before it is published in its final form, but we are providing this version to give early visibility of the article. Please note that, during the production process, errors may be discovered which could affect the content, and all legal disclaimers that apply to the journal pertain.

© 2022 Published by Elsevier Inc.

Materials Characterization, Volume 194, December 2022, Article number 112365
DOI: 10.1016/j.matchar.2022.112365

Journal Pre-proof

Strain hardening and strengthening mechanism of laser melting deposition (LMD) additively manufactured $FeCoCrNiAl_{0.5}$ high-entropy alloy

Lisong Zhu[a,b], Keping Geng[c], Jun Wang[d], Da Sun[b], Mengdie Shan[b], Yao Lu[a], Xuesong Zhang[b], Yangchuan Cai[b,*], Jian Han[a], Zhengyi Jiang[a,*]

[a]School of Mechanical, Materials, Mechatronic and Biomedical Engineering, University of Wollongong, Wollongong, NSW 2522, Australia

[b]School of Materials Science and Engineering, Tianjin University of Technology, Tianjin, 300384, China

[c]School of Mechanical Engineering, Tianjin Sino-German University of Applied Sciences, Tianjin, 300350, China

[d]Welding and Additive Manufacturing Centre, Cranfield University, Cranfield, Bedfordshire MK43 0AL, UK

***Corresponding authors:**

Yangchuan Cai, Email address: 18622265848@163.com

Zhengyi Jiang, Email address: jiang@uow.edu.au

Abstract: In order to develop the high-entropy alloy (HEA) with low cost and excellent mechanical properties for structural applications, the $FeCoCrNiAl_{0.5}$ HEA has been fabricated by laser melting deposition, one of the advanced additive manufacturing methods. Strain hardening behaviour has been analysed and discussed using the combination of characterisation techniques. The LMD-ed $FeCoCrNiAl_{0.5}$

Published by Elsevier. This is the Author Accepted Manuscript issued with: Creative Commons Attribution Non-Commercial No Derivatives License (CC:BY:NC:ND 4.0).
The final published version (version of record) is available online at DOI:10.1016/j.matchar.2022.112365. Please refer to any applicable publisher terms of use.

had a true yield strength and strain of 463 MPa and 2.94%. Also, the true tensile strength of the LMD-ed $FeCoCrNiAl_{0.5}$ reached 876 MPa, together with the ductility of ~24.97% (engineering strain). The LMD-ed $FeCoCrNiAl_{0.5}$ HEA exhibited a dual-phase structure of 93% face-centred cubic (FCC) phase and 6.9% ordered B2 phase. The phase boundary between the disordered FCC and ordered B2 phases played a key role in the barrier, which can block the movement of dislocations because of the lattice distortion, very large angle, and mismatch of the lattice. Dislocation pile-up and tangle caused the dislocation density near the phase boundaries to be higher than that in other areas, meanwhile, they further prevented the movement of dislocation under stress as they generated back stress, therefore LMD-ed $FeCoCrNiAl_{0.5}$ HEA had a good strain hardening behaviour with a strain hardening exponent of 0.92. This study provided an innovative insight into the development of HEAs with ordered phase by laser additive manufacturing for structural applications in extreme environments.

Keywords: High-entropy alloy; Laser melting deposition; Strain hardening; Phase boundary; $FeCoCrNiAl_{0.5}$

1. Introduction

High-entropy alloys (HEAs), also known as compositionally complex or multiple principal element alloys (MPEAs), were first proposed in 2004 [1, 2]. HEAs act in vast compositional space and reveal a lot of exciting properties which are different to

the traditional metallic materials, involving mechanical performance, corrosion resistance and thermal stability, and these properties make HEAs have good potentials in so many different applications [3-7]. However, it was reported that the advances of HEAs attained in the past more than ten years likely represent only the tip of the iceberg in the development of this promising class of alloys [8, 9].

However, balancing the applied performance and economic benefit does not seem to be an easy task. For instance, friction and re-manufacturing of components that failed by wear contacts, account for 23% of the global energy consumption with an estimated cost of over 2,500 billion Euro per year [10, 11]. This situation also occurs in HEAs with such good properties, which have a tremendous amount of probable alloying systems [12, 13].

For years microstructural control has always been seen as a significant strategy to modify the performances of the metallic materials. For the reduced activation ferritic/martensitic steels, the microstructures can be controlled to improve their mechanical properties under nuclear applications [14]. Microstructural control is still efficient to HEAs. For example, the heterogeneous structure produced by a simple process can considerably improve the mechanical properties of FeMnCoCr [15].

The coordination of chemical order and disorder can be controlled to improve the mechanical properties of metallic materials. With this strategy, the alloy with ordered superlattice structures and nanoscale disordered interfaces, which was designed by Yang et al. [16], can effectively avoid grain coarsening and softening at high

temperature, having a strength of 1.6 GPa and a ductility of 25%. Short-range order is an excellent strengthening strategy for HEAs, MPEAs, and medium-entropy alloys (MEAs). It is reported that the short-range order can be found in the CrCoNi MEA, and increased amounts of such order give rise to both higher stacking-fault energy and hardness [17]. Meanwhile, more and more studies showed that the arrangement of the atoms in HEAs was not an ideal disordered state, however, the generated short-range ordered structures during solidification or heat treatment processes due to the complex interactions between the constituent elements [18-20]. Manipulation of short-range order might provide better mechanical properties for HEAs [20]. For the $Fe_{40}Mn_{40}Co_{10}Cr_{10}$ HEA, the addition of boron with an adequate concentration resulted in deformation-induced short-range order, which causes severe lattice distortion, providing an increase of 210 MPa for the yield strength at low-temperature compared with boron-free reference materials [21]. It is noticed that the short-range order strengthening can break favourable bonds and increase the friction stress on gliding dislocations [22], contributing to the improvement in mechanical performances. Hence, by using the strengthening strategy of short-range order, the high cost of develop novel alloying system can be avoided.

Additive manufacturing (AM) [23, 24] is an advanced and modern manufacturing method. Compared with the traditional manufacturing and processing methods, less waste would be produced during this layer-by-layer manufacturing process, and such the waste can be reused in the next AM process. Therefore, AM

could be considered as an exciting manufacturing strategy, which provides a guarantee of sustainable production and reducing carbon emissions. Meanwhile, AM method can be used to fabricate the products with quite complex geometrical shapes quickly and directly [25-27], showing absolute superiority in comparison to traditional manufacturing methods such as casting and milling. Benefits from these characteristics, AM can be regarded as an important role in Industrial Revolution 4.0.

Nowadays, the laser AM methods have been used to prepare HEAs by researchers [28]. Laser melting deposition (LMD), one of the direct energy deposition AM techniques, especially suits the products with large scales and their mass production [29]. Satisfactory mechanical properties can be achieved in the LMD fabricated HEAs according to our previous studies [30]. $FeCoCrNiAl_x$ series HEAs are known as dual-phase alloy [31], providing excellent mechanical properties [32]. Herein, $FeCoCrNiAl_{0.5}$ HEA has been reported that it has a face-centred cubic (FCC) and B2 dual-phase structure [31, 33]. Since the B2 phase has an ordered body-centred cubic (BCC) lattice structure, the phases in $FeCoCrNiAl_{0.5}$ HEA can be divided into two states, i.e. disorder and order. The light atomic mass of Al not only provides the possibility for lightweight applications. Meanwhile, Al could be viewed as a protective element which gives oxidation resistance and corrosion resistance [34, 35]. Accordingly, the LMD-ed $FeCoCrNiAl_{0.5}$ HEA is expected to use as lightweight structural materials for special environments, such as aerocrafts, spacecrafts, wind turbine generators, etc

Strain hardening is a significant factor which is used to describe and reflect the mechanical property of a product under a practical service environment. The basic study indicates that $FeCoCrNiAl_{0.5}$ HEA fabricated by LMD technique has a good strength-ductility combination, however, the strain hardening mechanism of it is not clear [36].

Here, we fabricated $FeCoCrNiAl_{0.5}$ HEA with an ordered phase by LMD AM and evaluated its service performance based on strain hardening. Meanwhile, the strengthening mechanisms were discussed in detail with the combination of microstructures. The present study can facilitate a deep understanding of the strain hardening mechanism of $FeCoCrNiAl_{0.5}$ HEA. Also, we provided new insight into the selection and adjustment of HEAs which are used for additive manufacturing.

2. Experimental procedures

2.1. Materials and preparation process of LMD

In this study, 316 stainless steel (120 × 40 × 10 mm^3) was used as the substrate, and the specimen i.e. deposited wall, was fabricated on the surface of 316 stainless steel by LMD technique, as shown in Fig. 1a. The HEA powders in this experiment were prepared by the nitrogen atomisation method (supplier: Jiangsu Vilory Advanced Materials Technology Co., Ltd.). The designed molar ratio of the HEA powder used was 1 (Fe): 1 (Co): 1 (Cr): 1 (Ni): 0.5 (Al), and the powder purity was 99.0~99.5%. The chemical composition of the $FeCoCrNiAl_{0.5}$ HEA powders is listed in Table 1,

and the test standard referenced GB/T 14265 [37] and GB/T 23942 [38]. An NCS ONH-5500 O/N/H analyser was used to detect the contents of oxygen and nitrogen. The contents of oxygen and nitrogen were 51 ppm and 132 ppm, respectively. The particle size distribution of the $FeCoCrNiAl_{0.5}$ HEA powder ranged from 45 to 150 μm, here, D10=49.3 μm (size of 10% powders are not larger than 49.3 μm), D50=77.6 μm, and D90=122.0 μm, according to the test standard GB/T 19077 [39].

The surface of the substrate was ground using a milling machine, then it was cleaned with the acetone solution before LMD. The LMD system was used to fabricate the $FeCoCrNiAl_{0.5}$ HEA specimen (deposited wall), as shown in Fig. 1a. The LMD system mainly included a master control system (PLC S7-1200), a HANSGS-RJ0016-F3K fibre laser machine (manufacturer: Han's Laser Technology Industry Group Co., Ltd.), a KR22 R1610 robot arm (manufacturer: KUKA Robotics Manufacturing China Co., Ltd.), a coaxial powder feeding system (SF-02), and an argon chamber. In this study, the processing parameters for LMD were selected from our optimised processing parameter databases [40]: 1.06 μm laser wavelength; 1000 W laser power; 2 rpm transferring speed; 30 mm/min scanning speed. The deposited walls of $FeCoCrNiAl_{0.5}$ HEAs were produced by an ‘S’ type trajectory route at room temperature (25 ℃, 100 kPa), as shown in Fig. 1a. In this scanning strategy, the direction ‘X’ is the speed direction, namely transferring direction or transverse direction (TD), which was the horizontal path for the movement of the robot arm and laser beam; the direction ‘Y’ is the normal direction (ND), which was horizontal to

the workbench and normal to the side of the deposited wall; the direction 'Z' is the building direction (BD) for LMD in this study, which was the boosting direction for robot arm with a laser beam and was normal to the workbench. The deposition strategy was 'layer-by-layer', rising by a distance of 1 mm at the direction 'Z', i.e. BD, after depositing one layer, and the total number of deposited layers was 20. The shielding gas (Argon) flow rate was kept at 5 NL/min. Fig. 1b is the morphology of the cross-section of the product fabricated by LMD in this study. The deposited wall exhibited good formability, and no obvious defects (such as cracks and pores) can be found in the deposited wall.

Table 1 Accurate chemical composition of $FeCoCrNiAl_{0.5}$ powders (wt.%).

Elements	Al	Cr	Fe	Co	Ni
wt.%	5.81	22.26	23.17	24.34	24.42

2.2.Mechanical tests

An MTS SANS CMT5105 testing machine was used to conduct uniaxial tensile tests for the sample from the middle location of the HEA specimen at room temperature (25 ℃, 100 kPa). As shown in Fig. 1c, the dimensions of the reduced section of the tensile test sample were length × width × height = 20 mm × 1 mm × 1mm, and the loading rate was 1 mm/min. The test result has been compared to the previous report [36] to confirm the reliability. After that, an S-3400N SEM was used to observe the fracture morphology of the post-test tensile sample.

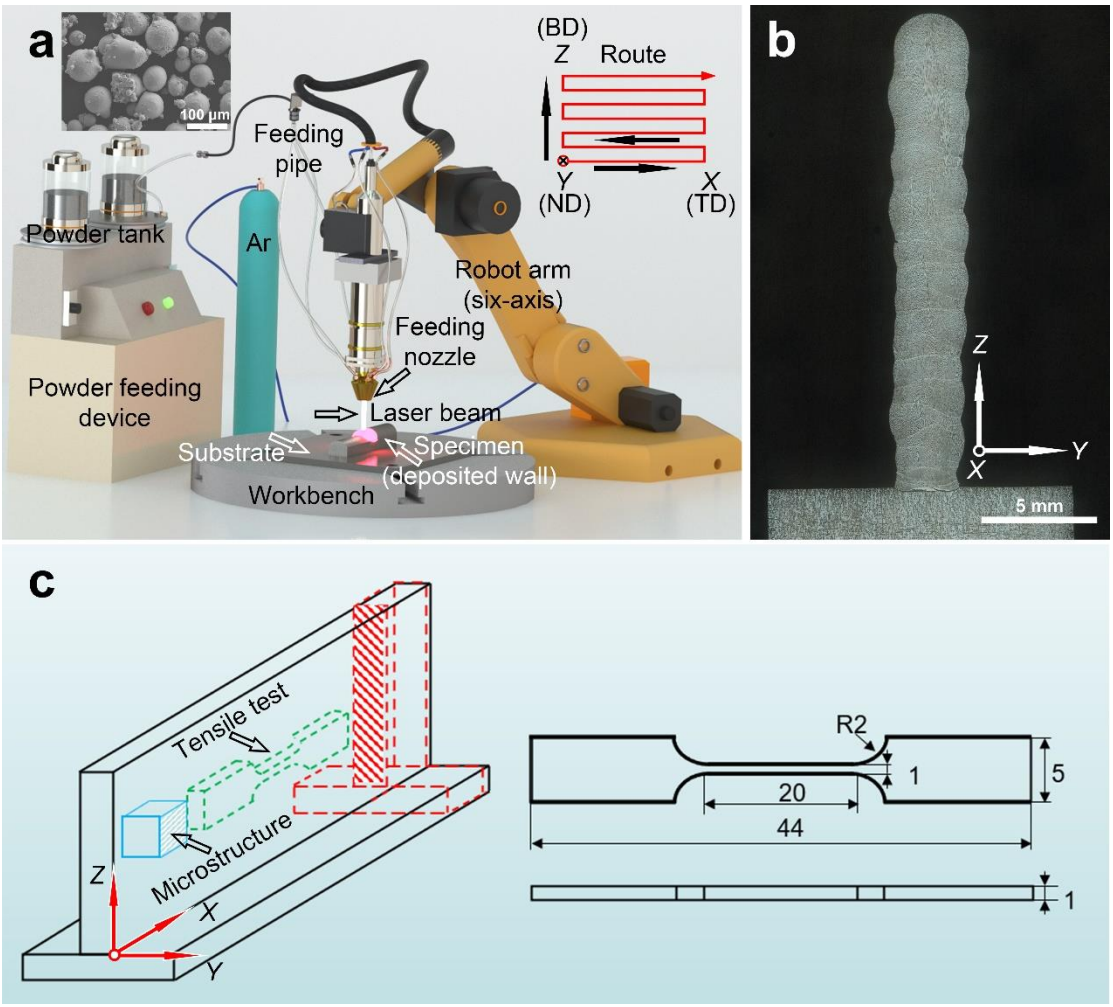


Fig. 1 (a) Schematic diagram of LMD system and processing route; (b) morphology of cross section (Y-Z plane); (c) schematic diagram of sampling.

2.3. Microstructure characterisation

All the samples for microstructural characterisation and mechanical property were taken from the middle locations of the X-Z plane of the LMD-ed $FeCoCrNiAl_{0.5}$ HEA specimen, as shown in Fig. 1c. The samples were subjected to grinding and polishing according to the standard procedures of metallography. After polishing, the samples were processed by electropolishing, and Electron Backscattered Diffraction (EBSD) analysis was conducted by a TESCAN MAIA3 SEM with a step size of 0.3

μm. To deeply characterise and analyse the microstructure, an FEI TECNAI F30 transmission electron microscope (TEM) was used to obtain high-magnification electron images, energy dispersive spectrometer (EDS) results, selected area electron diffraction (SAED) patterns, and high-resolution images (HR-TEM). The thickness of the TEM sample after electropolishing and Ar ion thinning was about 80 nm. The software Gatan Microscopy Suite® and CrysTBox [41] were applied to assist in the analysis of the detected results of TEM. The phase identification was carried out using a SmartLab advanced X-ray diffractometer (XRD, Rigaku D/max/2500PC) with a scanning speed of 3°/min and a range of 20° - 100°.

3. Results

3.1 Mechanical properties

Fig. 2a shows the true stress-strain curve of LMD-ed $FeCoCrNiAl_{0.5}$ HEA. The true yield strength of LMD-ed $FeCoCrNiAl_{0.5}$ HEA was 463 MPa in this study. Also, the true yield strain of LMD-ed $FeCoCrNiAl_{0.5}$ HEA from 2.94%.

The engineering stress and engineering strain results were shown in Table 2. The engineering yield strength and strain of LMD-ed $FeCoCrNiAl_{0.5}$ HEA were 450 MPa and 2.98%, respectively. Note that the engineering tensile strength and ductility of LMD-ed $FeCoCrNiAl_{0.5}$ HEA were 703 MPa and 24.97%, respectively. Therefore, in terms of both strength and plasticity, the $FeCoCrNiAl_{0.5}$ HEA fabricated by LMD has a good competitive performance no matter in theoretical design or practical service

environment.

When it comes to the strain hardening behaviour, the flow stress of a material in the uniform plastic deformation region is commonly expressed by the Hollomon relationship [42-45]:

$$\sigma_T = K\varepsilon_T^n \quad \text{(Eq. 1)}$$

where σ_T is the true stress, K is strength coefficient, ε_T is the true strain, and n is the strain hardening exponent. Strength coefficient and strain hardening exponent can be used to describe the strain hardening performance of the material, especially, the hardening exponent n is the main criterion to estimate the tensile performance. In some studies, the tensile curves could be fitted using the Ludwik equation [44, 46, 47]:

$$\sigma_T = \sigma_y + K\varepsilon^n \quad \text{(Eq. 2)}$$

where σ_y is the true yield strength of the material. Afrin et al. [48] reported that they evaluated the hardening exponent according to the following equation:

$$\sigma_T = \sigma_y + K(\varepsilon_T - \varepsilon_y)^n \quad \text{(Eq. 3)}$$

where ε_y is the true yield strain of the material. And the previous equation proposed by Afrin et al. [48] can be expressed in another way:

$$\sigma_T - \sigma_y = K(\varepsilon_T - \varepsilon_y)^n \quad \text{(Eq. 4)}$$

However, it is very hard to quickly calculate two constants, i.e. n and K, and visually illustrate their effect of them on strain hardening performance, according to the above equations. In the present study, the equation can be converted into a linear

form by taking the logarithm for each term:

$$\lg(\sigma_T - \sigma_y) = lgK + nlg(\varepsilon_T - \varepsilon_y) \quad \text{(Eq. 5)}$$

Through this formula, the transformed strength coefficient (lgK) and strain hardening exponent (n) can be fitted according to the true stress-strain data, and the strain hardening behaviours for LMD-ed $FeCoCrNiAl_{0.5}$ HEA can be displayed into two-liner function images, as shown in Fig. 2b. Noticeably, LMD-ed $FeCoCrNiAl_{0.5}$ has a higher strain hardening exponent (n) which provides the predominant contribution for strain hardening, and the value of n is 0.92 for LMD-ed $FeCoCrNiAl_{0.5}$ HEA. Hence, surely LMD-ed $FeCoCrNiAl_{0.5}$ HEA displays an obvious strain hardening behaviour after yield.

Also, because of strain hardening, the true tensile strength (876 MPa) of LMD-ed $FeCoCrNiAl_{0.5}$ HEA is almost close to twice as high as its true yield strength (463 MPa). At the same time, LMD-ed $FeCoCrNiAl_{0.5}$ HEA still provided an extra elongation ~19.36% (for true stain) during the strain hardening process after yield, as shown in Fig. 2a and Table 2. This guarantees that the LMD-ed $FeCoCrNiAl_{0.5}$ HEA can be applied as a structural material, since it can effectively avoid sudden failure and can continuously serve for a long term after yielding in theory, ensuring security to a large extent. For applications in extreme environments, this property is very meaningful.

Fig. 2c exhibits the micromorphology of tensile fracture observed by SEM. Besides the quasi-cleavages which were circled by yellow elliptical rings, there were

abundant dimples found in the fracture, which were marked in green circular rings, as shown in Fig. 2c. This micromorphology provides strongly positive evidence for the ductile fracture happening during the tensile test of LMD-ed $FeCoCrNiAl_{0.5}$ HEA, in other words, this material has reliable toughness. It is noticed that this situation also occurred in the process of strain hardening.

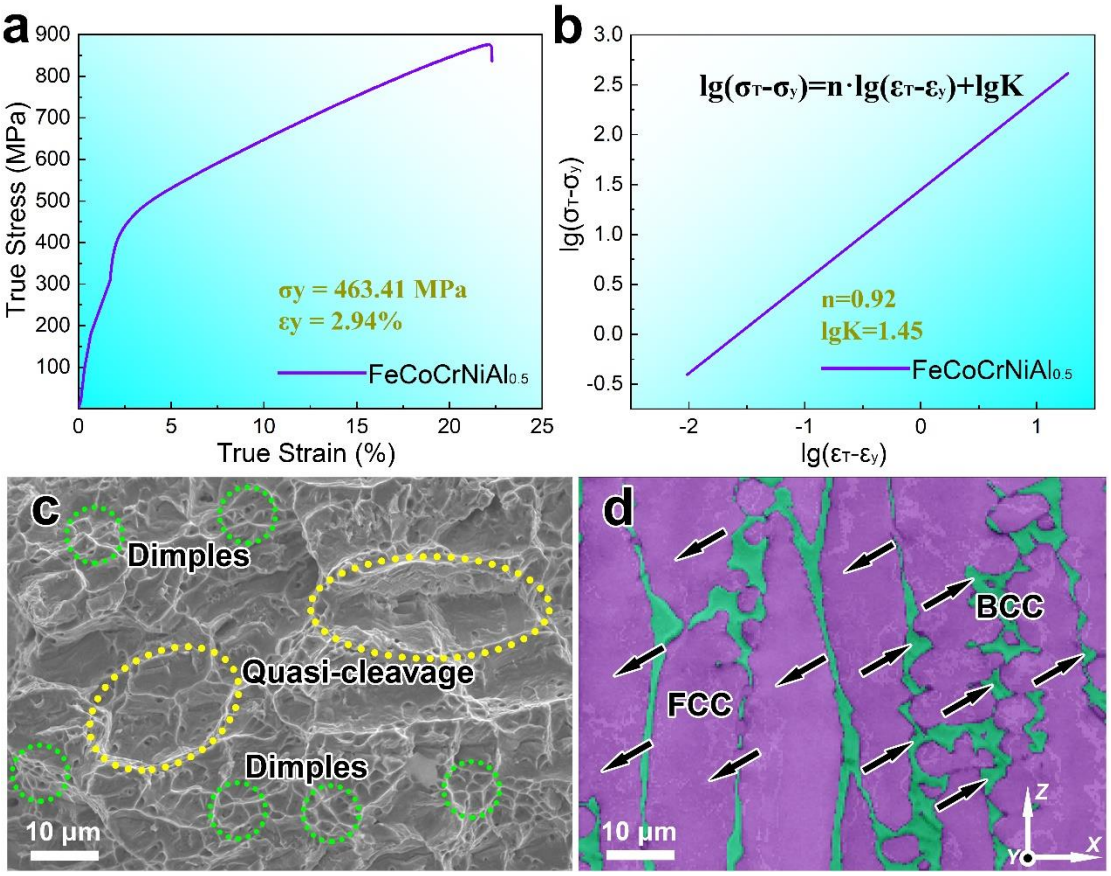


Fig. 2 Mechanical properties of LMD-ed $FeCoCrNiAl_{0.5}$: (a) true stress-strain curves and (b) fitted work hardening exponents (linear function images); microstructure: (c) SEM image of tensile fracture and (d) EBSD phase distribution image.

Table 2 Mechanical properties of LMD-ed $FeCoCrNiAl_{0.5}$ in this study.

$FeCoCrNiAl_{0.5}$ (as-LMD)	Value

Engineering yield strength	450 MPa
Engineering yield strain	2.98%
Engineering tensile strength	703 MPa
Ductility (engineering)	24.97%
True yield strength	463 MPa
True yield strain	2.94%
True tensile strength	876 MPa
Ductility (true)	22.30%
Strain hardening exponent (e)	0.92
Strength coefficient (lgK)	1.45

3.2 Microstructure characteristics

As shown in Fig. 2d, the high-power EBSD detection exhibits that there was a dual-phase characteristic of LMD-ed $FeCoCrNiAl_{0.5}$ HEA, all of the secondary phases were BCC phases, and the average grain size of the BCC phase zones was 7.95 μm (area-weighted mean). Especially, the shapes of BCC phase zones were irregular and inconsistent. The low-power EBSD detection result displays that the distribution of the secondary phase, i.e. BCC phase, was not particular, this means that the BCC phase zone could be randomly located at the interior of grain or the grain boundary in LMD-ed $FeCoCrNiAl_{0.5}$ HEA, as shown in Fig. S1 (Appendix A. Supplementary data).

To accurately identify each phase zone, thereby discussing the contribution and

influence of them on the properties of LMD-ed $FeCoCrNiAl_{0.5}$, the TEM detection for each phase zone has been given. The TME image of LMD-ed $FeCoCrNiAl_{0.5}$ in this study displays two significantly different zones, which were marked as ‘A’ and ‘B’, and there is a clear boundary between zone ‘A’ and zone ‘B’, as shown in Fig. 3a. To define the accurate phase types of zone ‘A’ and zone ‘B’, SAED of the two zones was given for three times by changing angles, respectively. Fig. 3 only gives two groups of SAED patterns for each zone, and the third SAED pattern group for the two zones are shown in Fig. S2 (Appendix A. Supplementary data). Please note that the measured interplanar spacings ‘A’, ‘B’, ‘C’, and ‘D’ for every SAED pattern were indicated in Table S1 (Appendix A. Supplementary data).

It is obvious that the lattice structure of zone ‘A’ was defined as FCC according to the SAED results, and the EDS results shown in Table 3 and Fig. S3 (Appendix A. Supplementary data) for zone ‘A’ indicated that the chemical composition of zone ‘A’ is disordered. Therefore, the phase of zone ‘A’ is a typical disordered FCC phase, this conforms to the general characteristic of the vast majority of HEAs. However, the EDS results for zone ‘B’ shows that the Al content was far higher than zone ‘A’. Besides, the SAED pattern of zone ‘B’ illustrates ordered superlattice diffraction patterns, where the incident electron beams *b*//<010> and *b*//<011> [49]. After analysing the interplanar spacings and angles measured from Figs. 3f, 3h and Fig. S2c, the closest phase-type of zone ‘B’ was Ni-Al intermetallic with BCC structure, namely the B2 phase. With the combination of the above characteristics of TEM

results and XRD pattern, the accurate phase-type of zone ‘B’ was identified as the ordered B2 phase. Hence, this local chemical fluctuation of the $FeCoCrNiAl_{0.5}$ HEA fabricated by the LMD technique in this study matches the characteristic of ‘long-range disorder and short-range order’.

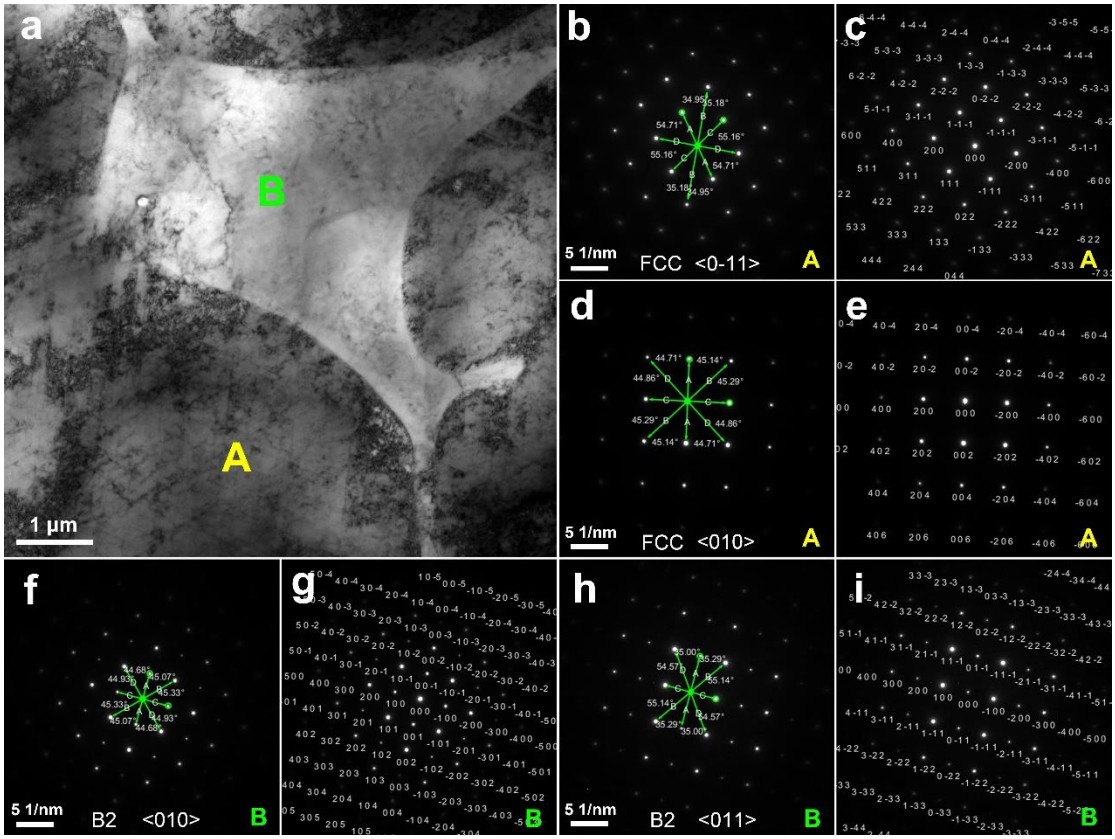


Fig. 3 (a) TEM image of LMD-ed $FeCoCrNiAl_{0.5}$ HEA; (b-e) SAED patterns of zone ‘A’ in (a); (f-i) SAED patterns of zone ‘B’ in (a).

Table 3 EDS results of zone ‘A’ and zone ‘B’ in Fig. 3a.

Element Proportion (Atomic %)					
Area	Al	Cr	Fe	Co	Ni
A (FCC)	8.63	24.56	21.55	21.44	23.80

B (B2)	18.69	20.88	16.99	20.26	23.15

The lattice parameter for cubic lattice can be calculated according to the following equation:

$$d = \frac{a}{\sqrt{h^2+k^2+l^2}} \quad \text{(Eq. 6)}$$

where d is the interplanar spacing, and a is the lattice parameter. According to Figs. 3 and S2, and Table S1, the calculated lattice parameters for The FCC phase and B2 phase in this study are 3.516 Å and 2.808 Å, respectively. The shortest interatomic distance for the FCC lattice is in <110>, and it is in <111> for the BCC lattice. With using of the value of the lattice parameter, the Burgers vector $|b|$ for the FCC lattice and BCC lattice can be calculated by the following two equations, respectively:

$$|b|_{FCC} = \frac{\sqrt{2}}{2}a \quad \text{(Eq. 7)}$$

$$|b|_{BCC} = \frac{\sqrt{3}}{2}a \quad \text{(Eq. 8)}$$

Here, the Burgers vector $|b|$ of FCC phase in this study was 0.2486 nm, for the B2 phase, it was 0.2431 nm. According to the Burgers vectors, the density of geometrically necessary dislocation (GND) for the two phases could be calculated. Figs. 4a and 4b show the distribution of GND in FCC phase zones and B2 phase zones, respectively. Clearly, the dislocations in grains distributed randomly without distinguishing features. However, it is noteworthy that the density of GND of the FCC phase at phase boundaries is far more than the other zones, as shown in Fig. 4a. When it comes to the B2 phase zones, as shown in Fig. 4b, it is very difficult to sum up a representative distribution characteristic.

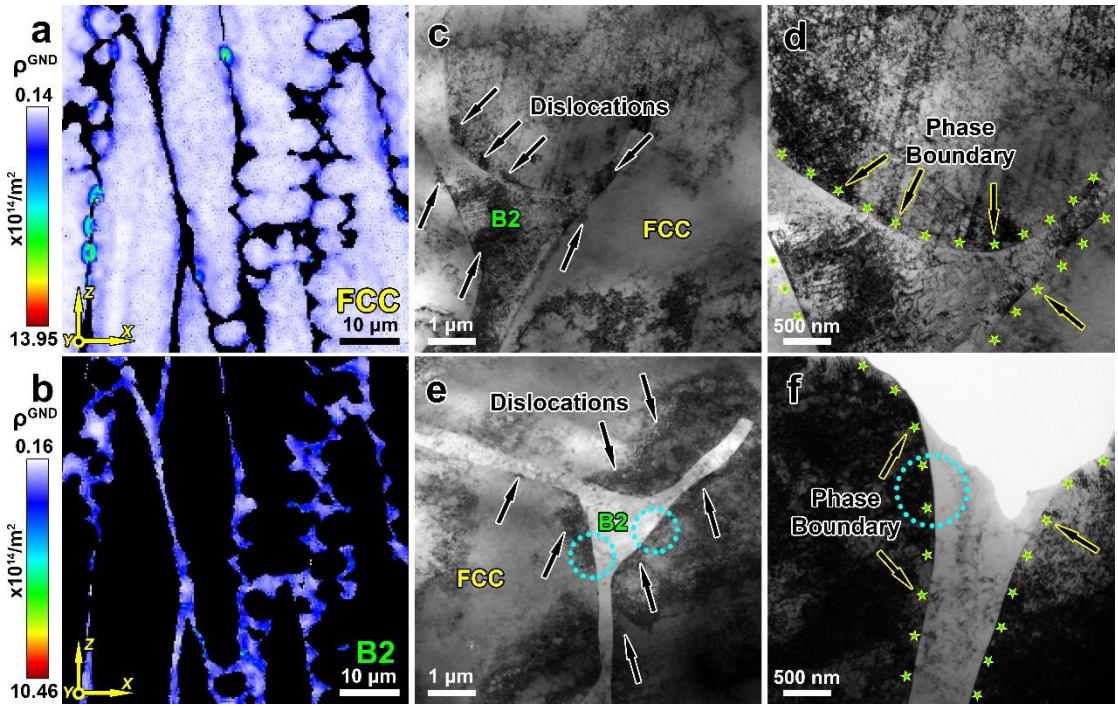


Fig. 4 (a) Distribution of GND density in FCC phase zones; (b) distribution of GND density in B2 phase zones; (c-f) TEM image showing dislocations distributions and phase boundaries: (d) is the local magnification of (c), (f) is the local magnification of (e).

According to Figs. 4 (c-f), the TEM images for B2 phase zones and FCC zones clearly illustrate a large number of dislocations are located at phase boundary zones. The density of dislocations at the side of FCC near the phase boundary is far more the other side i.e. B2 zone, which has hardly any dislocations, and this situation is displayed in the zones which are marked by the blue circle in Figs. 4e and 4f. Although the shapes of the B2 phase zone are irregular and inconsistent, the same condition which is dislocations seriously stacking at the FCC side near the phase

boundary also can be recognised, as shown in Fig. S4. In addition, Fig. S4 indicates that the equivalent diameters of the B2 phase zone are less than 10 μm, this is the same to the result of Fig. 2d. In summary, according to the results of EBSD and TEM detection, it is clearly and directly recognised that there were a fairly lot of dislocations stacking at phase boundaries in FCC phase zones, and the density of dislocation at phase boundaries is far more than that of other areas.

To study the phase boundary zones more clearly and deeply, we gave the HR-TEM detection of them. The FFT pattern of Figs. 5b and 5d show that the phase types of zone 'A' and zone 'B' are FCC and B2, respectively. The clearer FFT pattern in Fig. 5a is given in Fig. S5 (Appendix A. Supplementary data). The IFFT lattice fringe (Fig. 5c) on {-111} illustrates a lot of <-111> dislocations at the FCC zone nearby the phase boundary. Similarly, there are a significant number of <1-10> dislocations at the B2 zone nearby the phase boundary, as shown in Fig. 5e. As for the joint zone of the FCC phase and B2 phase, the visible dislocation density is much higher than that on the two sides.

The FFT pattern for Fig. 5a zone exhibits that the {111} of the FCC phase is not parallel to the {110} of the B2 phase in the orientation of $<0\text{-}11>_{FCC}//<001>_{B2}$, thus, the Kurdjumov-Sachs (K-S) crystallographic relationship [50] could not appear in this zone. Therefore, the coherent interface between FCC zone and B2 zone with BCC structure could not be formed. However, we noticed that the angle between FCC's

{200} and B2's {020} is pushing 0 °, this indicates $\{200\}_{FCC}//\{020\}_{B2}$.

However, because of the too large mismatch (more than 14%) of phase boundary, the coherent lattice does not exist at the interface on {200} of FCC and B2. Here, the ineffective crystal orientation and too large mismatch occur it is very hard to dislocations to move through the interface, therefore a lot of dislocation motions would be blocked at the two sides of grain boundaries. Meanwhile, the serious lattice mismatch also results in the generation of a large number of dislocations, this is the reason why the dislocation density at the phase boundary zone is much higher than is at the zone far from the boundary, which is shown in Figs. 4 and S4. In addition, the IFFT lattice fringe in Fig. 5f exhibits that there are such obvious lattice distortions at the joint zone of the FCC and B2 phases. What needs to be highlighted is that the serious lattice distortion increases the internal energy and micro stress on the material, this is also a huge barrier which stops the dislocation's motions. Accordingly, dislocation pile-up might occur at sides of phase boundaries under stress and strain.

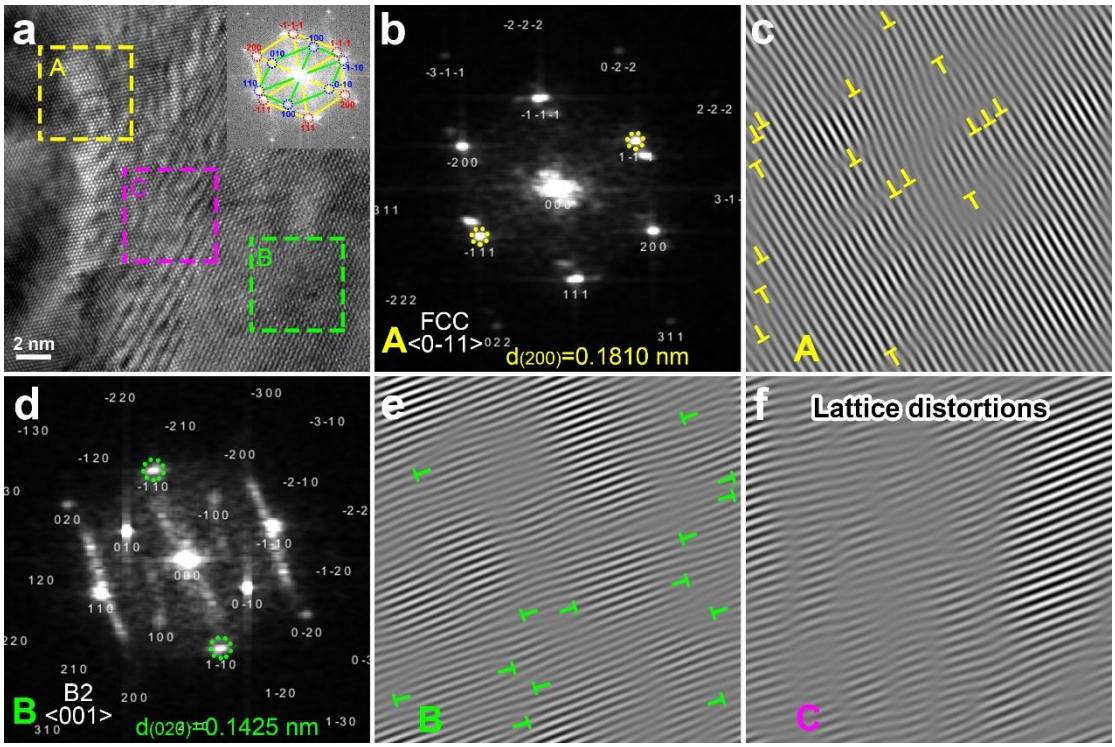


Fig. 5 (a) HR-TEM image with FFT pattern of FCC-B2 phase boundary; (b) FFT pattern of FCC-zone 'A' in (a); (c) IFFT lattice fringe of FCC-zone 'A' based on the marked spots in (b); (d) FFT patterns of B2-zone 'B' in (a); (e) IFFT lattice fringe of B2-zone 'B' based on the marked spots in (d); IFFT lattice fringe of boundary-zone 'C' in (a).

Fig. 6 shows a phase boundary zone with K-S relationship, i.e. $\{111\}_{FCC}//\{-1-10\}_{B2}$ and $<001>_{FCC}//<0-11>_{B2}$ in this study. Although the K-S relationship has been confirmed in this phase boundary, the too-large mismatch which was calculated according to the interplanar spacing of (200) of FCC phase and B2 phase in this study, was up to 14%, the complete coherent interface still cannot appear in this area. Despite this, because of the important role of the K-S relationship at this phase boundary, and lattice distortions at this phase boundary are not very visible,

these provide favourable conditions for the movement of dislocations breaking through the phase boundary, they are different to the phenomena in Fig. 6. While, as mentioned just now, owing to the mismatch of phase boundary, the K-S relationship will not play quite a perfect role as expected. Accordingly, in the phase boundary zones with explicit K-S relationship, but they're only a part of dislocations can move break through the phase boundary, and another part is still blocked at the two sides of the phase boundary.

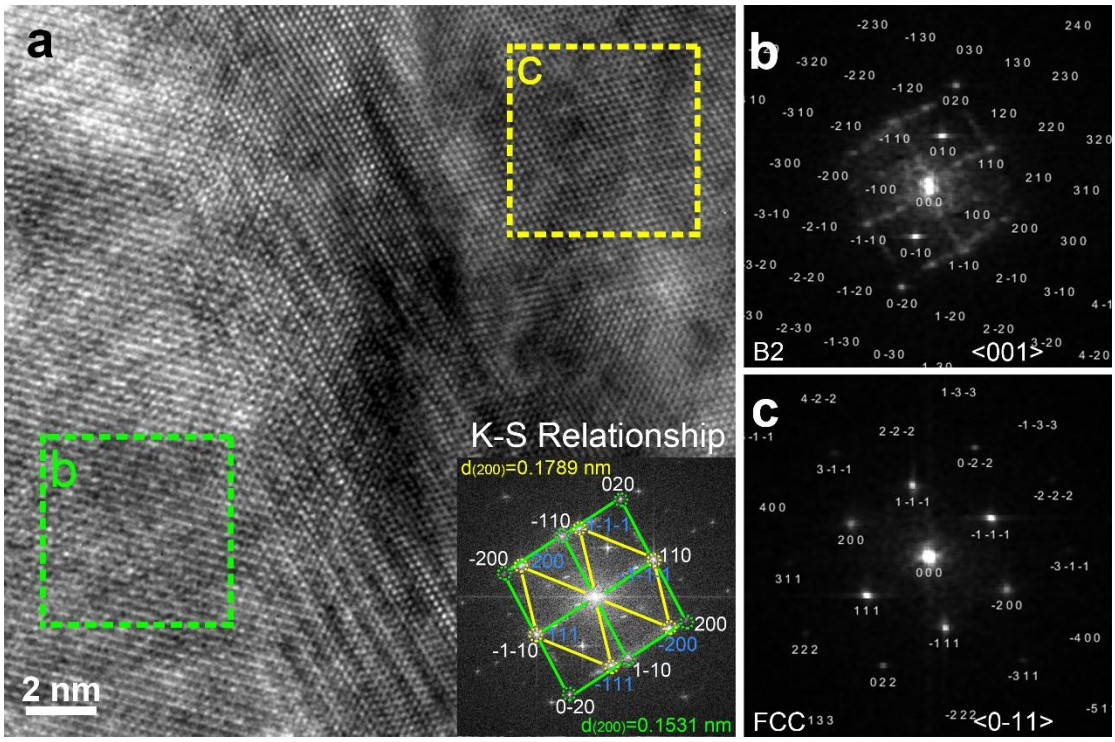


Fig. 6 (a) HR-TEM image of FCC-B2 phase boundary with FFT pattern; (b) FFT pattern of B2-zone in (a); (c) FFT pattern of FCC-zone in (a).

Fig. 7 gives another situation of the phase boundary. An obvious demarcation between the FCC phase and B2 phase can be seen in the HR-TEM of phase boundary, as shown in Fig. 7a. The main reason why this phenomenon occurs is essentially the

too large angle between the FCC phase and the B2 phase. Here, the phase boundary plays a role as well as the grain boundary. Under this situation, the dislocation pile-up will be more obvious and more serious than other types of phase boundaries which were displayed in Figs. 5 and 6. Therefore, Figs. 7b and 7c indicate that quite a lot of dislocations are located at the side of the FCC phase, but there is little or no dislocation in the B2 phase side nearby the phase boundary. This is because the dislocation totally cannot move breaking through this type of phase boundary, thereby a crowd of dislocations of the FCC phase were blocked by the phase boundary, unable to disturb the B2 phase zone on the other side. This phenomenon is reflected in the areas marked by blue circles of Figs. 4e and 4f.

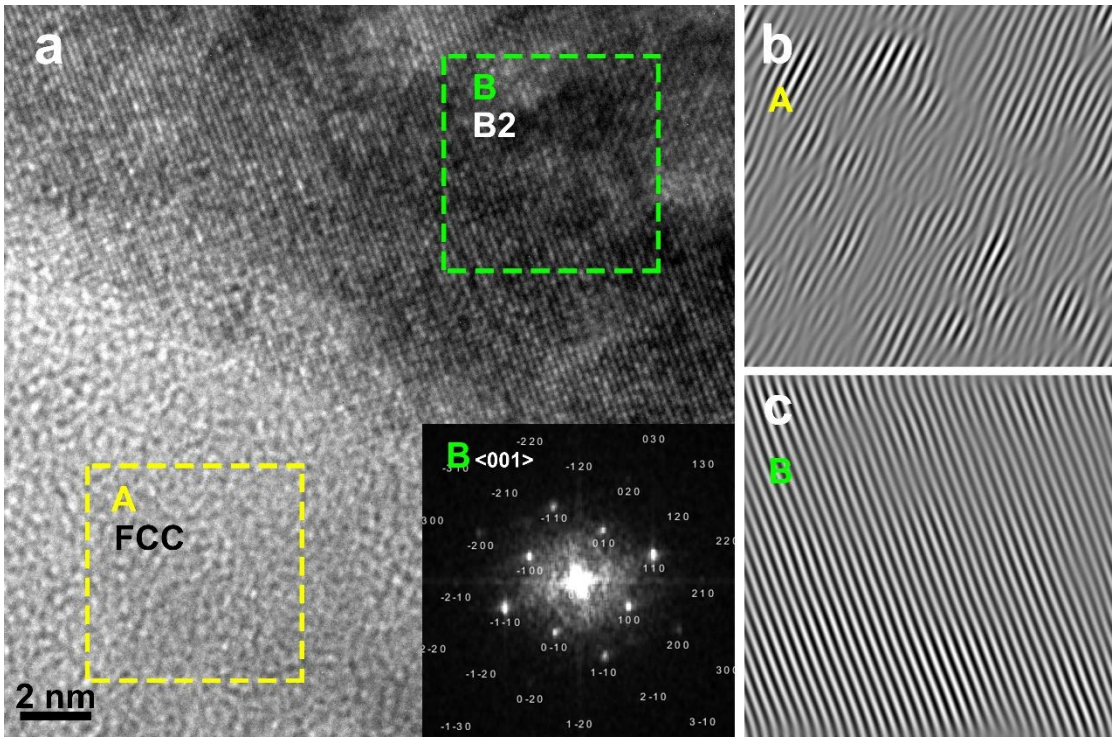


Fig. 7 (a) HR-TEM image of FCC-B2 phase boundary with FFT pattern of B2-zone 'B'; (b) IFFT lattice fringe of FCC-zone 'A' in (a); (c) IFFT lattice fringe of B2-zone 'B' in (a).

As mentioned earlier, there is no fixed shape of the B2 phase zone (Figs. 2 and S4). However, the crucial role of phase boundary is almost unaffected by the shape of the B2 phase zone, because of the given lattice parameters of FCC and B2 phases, and the angle between the crystal of the two phases, resulting in the generation of phase boundary, altogether. Hence, the very slender and thin B2 phase zone can still be seen as a great barrier which can block the movement of the vast majority of dislocations, this situation is shown in Fig. 8a. The image of local magnification of this phase boundary, which is given in Fig. 8b, exhibited a lot of obvious dislocation tangles. This condition will contribute a positive effect on the mechanical property.

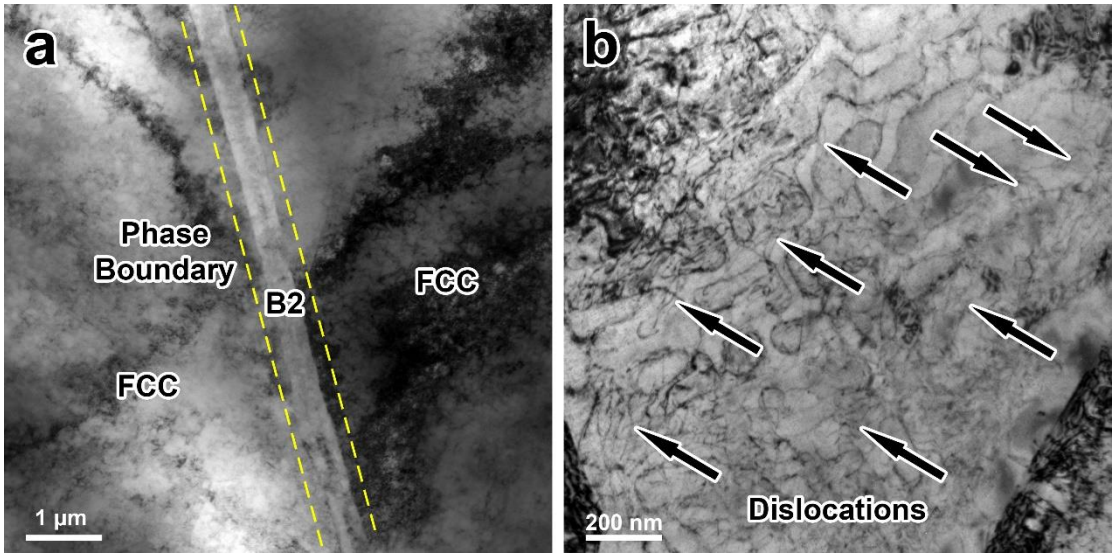


Fig. 8 (a) TEM image of slender B2-zone and phase boundary; (b) TEM of dislocation tangle at the grain boundary.

4. Discussions

A report from Liu et al. [51] demonstrated that the valence electron concentration

is a critical factor for regulating the phase transformation in HEAs, and the electronic redistribution is the essence which promotes this transformation. Recently, more and more scholars tended to adopt simulation methods to discuss the phase content and its effects on the performances of HEAs, such as the Monte Carlo method, molecular dynamics, and first-principles calculation. Chen et al. [52] used the Monte Carlo method, molecular dynamic simulation, and density-functional theory calculation to study CoCuFeNiPd HEA. It is reported that this HEA is energetically favourable to undergo short-range ordering, thus enhancing the strength and ductility [53].

Santodonato et al. [31] reconstructed the formation of the B2 phase in Al-content HEAs under special physical conditions using Monte Carlo method, building in the enthalpies associated with forming ordered phases. The interactions between different alloy elements played a significant role in the formation of different phases including the ordered B2 phase [31]. For the HEAs, B2 precipitates can be used to improve the mechanical properties including fatigue life, which is attributed to the high elasticity, plastic deformability, and martensitic transformation of the B2-strengthening phase [32]. Also, the B2 phase played a significant role in the enhancing mechanism of the material in this study. The rapid solidification during the LMD process, a large number of dislocations can generate during this process [30] whose effects on work hardening is crucial [53], hence the discussion of the relationship between dislocation, phase structure and strain hardening is necessary.

The dislocation density can be estimated from the XRD pattern

(PDF#97-015-0607 for B2 phase) in Fig. 9, using the Williamson-Hall method [54, 55], which can be expressed by the following equation:

$$\frac{\delta_{hkl}cos\theta_{hkl}}{\lambda} = \frac{1}{D} + \frac{4esin\theta_{hkl}}{\lambda} \quad \text{(Eq. 9)}$$

where δ_{hkl} is the full width at half maximum (FWHM) of the diffraction peak, θ_{hkl} is the diffraction angle at the peak, λ is the X-ray wavelength, D is the average size of the coherently diffracting domains, and e is the effective mean microstrain. Here, the effective mean microstrain can be calculated by the following equation, which is the fitted slope according to different diffraction peaks:

$$e = \frac{\Delta(\delta_{hkl}cos\theta_{hkl})}{\Delta(4sin\theta_{hkl})} \quad \text{(Eq. 10)}$$

In this study, the FWHM were 0.021°and 0.253° for the FCC phase, and the diffraction angle was 43.483° and 50.657° for the (111) and (200) FCC phase, which are the two most obvious diffraction peaks of the FCC phase in Fig. 9. Also, for the B2 phase, the FWHM of (111) and (210) were 0.048° and 0.506°, and the diffraction angles were 44.515° (111) and 64.920° (210), respectively. Subsequently, the ρ is calculated by the following formula [56, 57]:

$$\rho = 14.4\frac{e^2}{b^2} \quad \text{(Eq. 11)}$$

where b is the Burgers vector, and the revised Burgers vectors for the FCC and the B2 phases were 0.2486 nm and 0.2431 nm, respectively, according to Fig. 3. Hence, the dislocation density (ρ) was calculated to be ~3.64 × 10^{14}/m^2 and ~3.97 × 10^{15}/m^2 for the FCC and B2 phases, respectively.

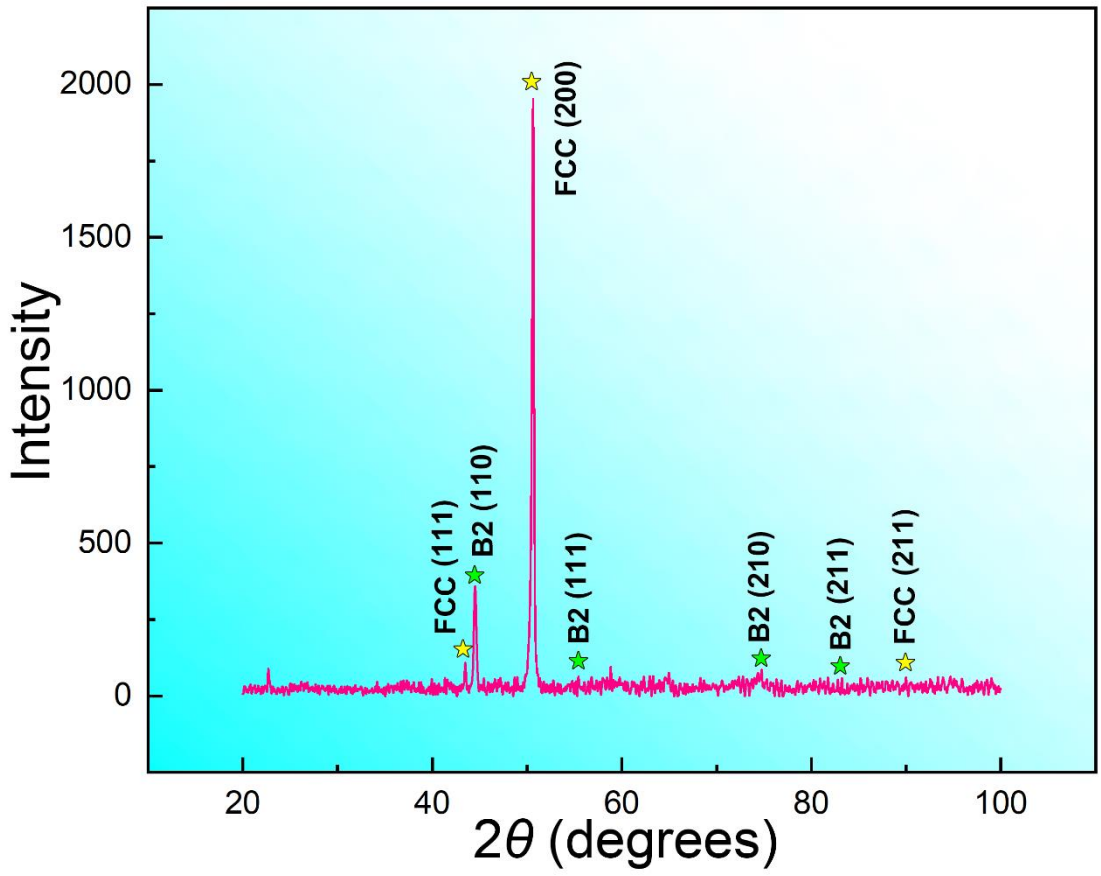


Fig. 9 XRD pattern of LMD-ed $FeCoCrNiAl_{0.5}$ HEA.

The heat accumulation during additive manufacturing caused the epitaxial growth and preferred orientation of the coarse columnar grains, as shown in the EBSD result in Fig. S1 and the XRD result shown in Fig. 10, therefore Hall-Petch relation cannot produce a marked effect here. The dislocation strengthening (σ_{SH}), can be described by the following equation [58]:

$$\sigma_{SH} = M\alpha Gb\rho^{\frac{1}{2}} \quad \text{(Eq. 12)}$$

where $M = 3.06$ is the Taylor factor [59], and $\alpha = 0.2$ is the constant for FCC metals [60, 61]. As indicated in Table 3, because of the existence of the B2 phase with high content of Al element, the real proportion of alloying elements in the FCC phase is about 1 (Fe): 1 (Co): 1 (Cr): 1 (Ni): 0.3 (Al), therefore, $G = 80\ GPa$is the shear

modulus of $FeCoCrNiAl_{0.3}$ HEA [57, 61], which is approximately equal to the FCC phase in this study.

Hence, the dislocation strengthening from the FCC phase contributed ~242 MPa for LMD-ed $FeCoCrNiAl_{0.5}$ HEA in this study. Dislocation strengthening is the most important factor in strain hardening. However, the true stress-strain curve shown in Fig. 2b illustrates that LMD-ed $FeCoCrNiAl_{0.5}$ provided a strain hardening of ~412 MPa, which is far higher than the calculated dislocation strengthening value. In addition, the EBSD result in Fig. S1 shows that the proportion of the B2 phase in this study was only 6.9%, and the proportion of the FCC phase was 93%, thus, the role of dislocation strengthening from the B2 phase was very slight, only contributing a very little value to the true strength.

In addition, B2 phase acts a role as precipitation strengthening, whose contribution can be calculated by Orowan equation [62]:

$$\sigma_P = 0.538 \frac{Gbf_P^{1/2}}{D_P} \ln\left(\frac{D_P}{2b}\right) \quad \text{(Eq. 13)}$$

where D_P and f_P are the average grain size and phase fraction of the precipitates respectively, in this study, $D_P = 7.95\,\mu m$ and $f_P = 6.9\%$; $G = 80\,GPa$ and $b = 0.2486\,nm$ are the shear modulus and Burgers vector respectively, which were used in dislocation strengthening calculation. Hence, B2 phase provided ~148 MPa of precipitation strengthening. Note that the precipitation strengthening originates from the interaction of dislocations and precipitated phase. Because of the incoherent interface between the FCC and B2 phases in this study, the role of precipitation

strengthening can be reflected under stress.

Fig. 10 is the simulated diffraction pattern, which indicates the orientation relationships in Figs. 5 and 6. As shown in Fig. 10a, at the zone axis $[001]_{B2}//[0\text{-}11]_{FCC}$, when the (110) of the B2 phase is parallel to the (-1-1-1) of the FCC phase, the K-S relationship is established under this situation. Theoretically, the coherent interface can form at the boundary with the K-S relationship. Nevertheless, the mismatch between the lattice parameters of the B2 and FCC phases is more than 14%, which means that a completely effective coherent interface cannot appear in this area. Although a small number of dislocations can move through the phase boundary with the K-S relationship, the vast majority of dislocations are still blocked by this boundary. Differently, Fig. 10b demonstrates an orientation between the B2 and FCC phases, which does not meet the K-S relationship or N-W relationship, the coherent interface cannot appear in theory. Even though the (020) of the B2 phase is parallel to the (-200) of the FCC phase, the too-large mismatch results in the phase boundary under this situation being incoherent. Hence the serious lattice distortion and a lot of dislocations can be found in this area, in other words, there is a large barrier to block the movement of dislocations.

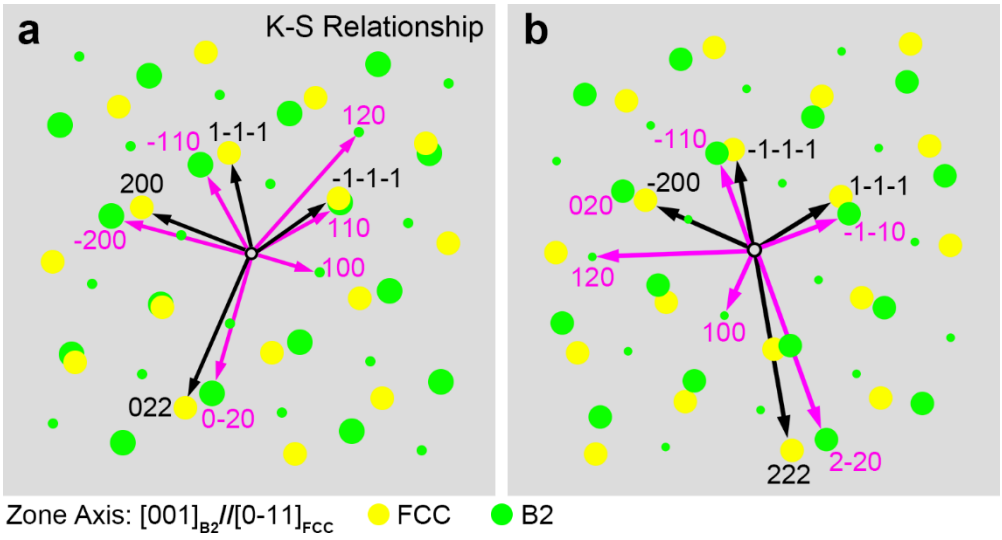


Fig. 10 Simulated diffraction pattern of phase boundary at the zone axis $[001]_{B2}//[0\text{-}11]_{FCC}$.

Also, if there is a large angle between the two phases, i.e. FCC and B2, a very obvious demarcation between the two phases. Fig. 11 reveals that dislocations located at FCC phase zone hardly move from one side to the other side breakthrough the phase boundary. With this condition, although one of the two sides has little or no dislocations, and the other side has a large number of dislocations, the dislocations at one phase zone still cannot disturb the adjacent phase zone without any dislocations. This situation is displayed in Fig. 7, and the circled zone of Figs. 4e and 4f. Different to the above two situations in Figs. 5, 6 and 10, it is nearly impossible that dislocations move through this type of phase boundary. Therefore, the dislocation pile-up near this type of phase boundary will be more serious.

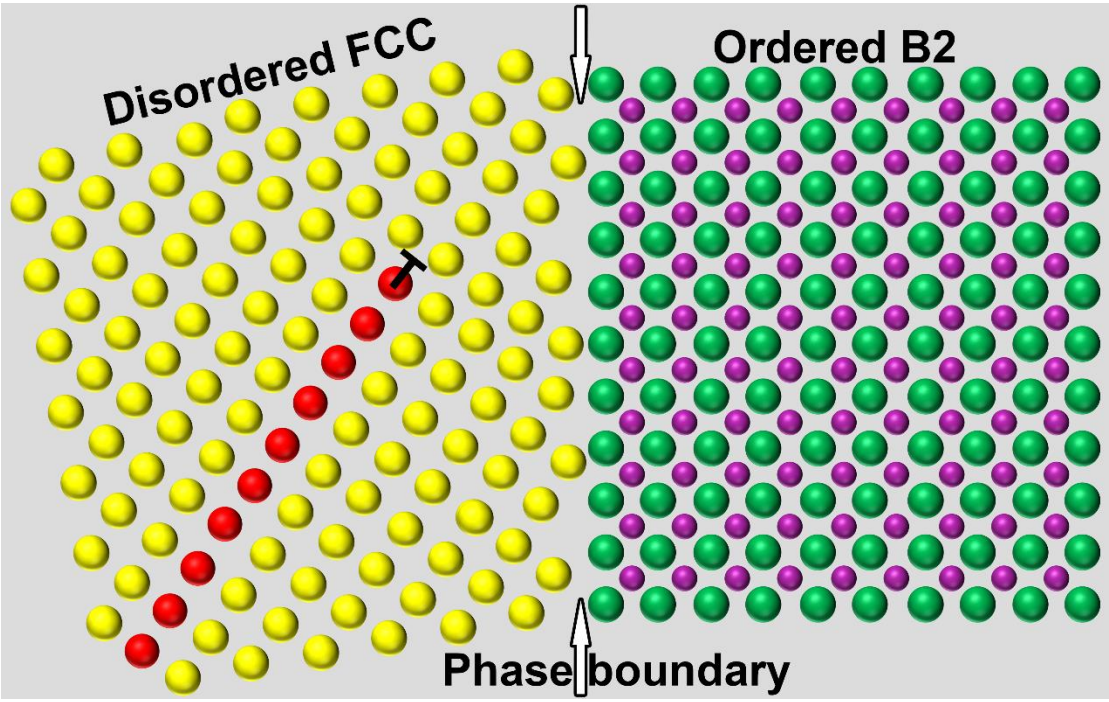


Fig. 11 Atomic diagram at phase boundary.

Fig. 12 gives the diagram of the strain-hardening mechanism of LMD-ed $FeCoCrNiAl_{0.5}$ HEA in this study. It is clear that there are a lot of dislocations in the LMD-ed sample, because of the high cooling rate characteristic of the LMD technique. Dislocations are uniformly distributed in intragranular FCC phase zones. What needs to be highlighted is that the dislocation density nearby the phase boundary is far more than in other areas. Under the deformation caused by stress, the material can provide more than 230 MPa dislocation strengthening. However, the B2 phase with the characteristic of chemical order plays a significant role in precipitation strengthening. Here, dislocations result in a continuous strain hardening effect. Owing to the influence of the boundary between the FCC and B2 phases, most of the dislocations which move to phase boundaries under stress will be blocked, thereby leading to the phenomenon of serious dislocations pile-up and tangle. The pile-up and tangle of

dislocations will generate back stress [63, 64], which further blocks the movement of dislocations, this makes the deformation very difficult and provides a higher strain hardening effect, as shown in Figs. 2a and 2b. Meanwhile, the significant dislocation pile-up resulted in the dislocation multiplication during plastic deformation, which further enhanced the strain hardening. As a result, the LMD-ed $FeCoCrNiAl_{0.5}$ HEA has higher strain hardening rate than that of the traditional HEA such as FeCoCrNi [30]. Under the extreme application environments, such as nuclear industry, aerospace and defense facility, the high strain-hardening behaviour of LMD-ed $FeCoCrNiAl_{0.5}$ HEA will provide good reliability and safety.

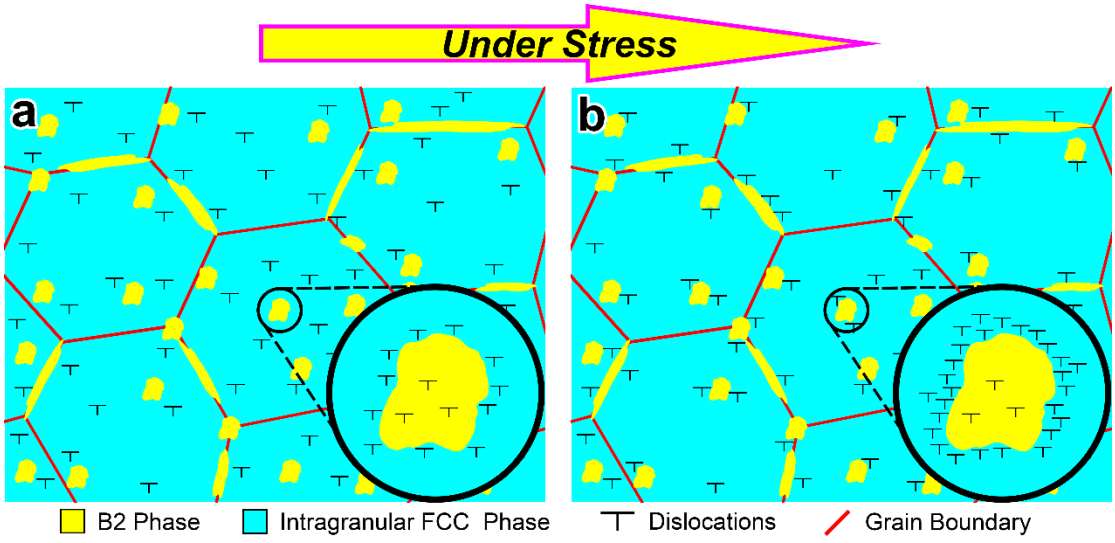


Fig. 12 Diagram of the strain-hardening mechanism of LMD-ed $FeCoCrNiAl_{0.5}$ HEA: (a) before stress; (b) under stress.

5. Conclusions

The $FeCoCrNiAl_{0.5}$ HEA has been fabricated by the LMD additive manufacturing technique, and the strain hardening and strengthening mechanisms

have been discussed as focusing on the phase boundary and dislocation motion regular. We provided further evidence for the application of HEAs with ordered phase manufactured by the LMD technique on structural materials in this study. Meanwhile, the results can be considered as a guidance for the development HEAs with ordered phase for laser additive manufacturing, as well as an instructive strategy for improving traditional HEAs. The detailed conclusions are as follows:

(1) The LMD-ed $FeCoCrNiAl_{0.5}$ high-entropy alloy is fabricated by LMD additive manufacturing has a ~876 MPa true tensile strength, a ~463 MPa true yield strength, a ~19% true ductility, and a hardening exponent of 0.92, revealing a satisfactory strain hardening behaviour and toughness.

(2) The LMD-ed $FeCoCrNiAl_{0.5}$ high-entropy alloy has a lot of disordered FCC phase zones (with a content of 93%) and a few ordered B2 phase zones (with a content of 6.9%), exhibiting a characteristic of ‘long-range disorder and short-range order’.

(3) The distribution of the chemical ordered B2 phase is mainly random, and a lot of B2 phases were found at grain boundaries. Dislocations are uniformly distributed in grains, and the serious lattice mismatch between the FCC and B2 phases cause higher dislocation density nearby the phase boundary.

(4) Under stress-strain, serious lattice mismatch, too large angle, and significant lattice distortion of phase boundary blocked the movement of locations. Also, dislocations still could not effectively move through the interface with the K-S

relationship because of lattice mismatch.

(5) Owing to the barrier role of phase boundary, significant dislocation pile-up and tangle occurred at the two sides of phase boundaries, where the back stress and dislocation multiplication provided higher strain hardening.

Acknowledgements

The lead author L.S. Zhu from University of Wollongong and Tianjin University of Technology made the main contributions to this study. Special thanks to these authors for their significant contributions: the second author K.P. Geng from Tianjin Sino-German University of Applied Sciences mainly contributed to manipulating the LMD system; co-author J. Wang from Cranfield University provided useful analysis, discussion and editing for this study; co-authors D. Sun and M.D. Shan from Tianjin University of Technology did great efforts for relevant experiments. The authors are very grateful for relevant device support from Tianjin Sino-German University of Applied Sciences. This work was mainly supported by Advanced Materials Processing and Manufacturing Research Institute, School of Materials Science and Engineering, Tianjin University of Technology. The author J. Han from University of Wollongong provided funding support for this project. This work was also funded by National Natural Science Foundation of China (Grant No: 52205409) and Enterprise Science and Technology Commissioner Project (Grant No: 22YDTPJC00310).

Data availability

The data in this paper and our process parameter databases can be provided on reasonable requests. Please address to corresponding authors (Dr Yangchuan Cai and Prof Zhengyi Jiang) for requests.

References

[1] J.W. Yeh, S.K. Chen, S.J. Lin, J.Y. Gan, T.S. Chin, T.Y. Shun, C.H. Tsau, S.Y. Chang, Nanostructured high-entropy alloys with multiple principal elements: novel alloy design concepts and outcomes, Adv. Eng. Mater. 6 (2004) 299-303. https://doi.org/10.1002/adem.200300567.

[2] B. Cantor, I.T.H. Chang, P. Knight, A.J.B. Vincent, Microstructural development in equiatomic multicomponent alloys, Mater. Sci. Eng. A 375-377 (2004) 213-218. https://doi.org/10.1016/j.msea.2003.10.257

[3] E.P. George, W.A. Curtin, C.C. Tasan, High entropy alloys: A focused review of mechanical properties and deformation mechanisms, Acta Mater. 188 (2020) 435-474. https://doi.org/10.1016/j.actamat.2019.12.015.

[4] Y. Fu, J. Li, H. Luo, C.W. Du, X.G. Li, Recent advances on environmental corrosion behavior and mechanism of high-entropy alloys, J Mater. Sci. Technol. 80 (2021) 217-233. https://doi.org/10.1016/j.jmst.2020.11.044.

[5] J.Y. Pang, H.W. Zhang, L. Zhang, Z.W. Zhu, H.M. Fu, H. Li, A.M. Wang, Z.K. Li, H.F. Zhang, A ductile $Nb_{40}Ti_{25}Al_{15}V_{10}Ta_5Hf_3W_2$ refractory high entropy alloy with

high specific strength for high-temperature applications, Mater. Sci. Eng. A 831 (2022) 142290. https://doi.org/10.1016/j.msea.2021.142290.

[6] E.P. George, D. Raabe, R.O. Ritchie, High-entropy alloys, Nat. Rev. Mater. 4 (2019) 515–534. https://doi.org/10.1038/s41578-019-0121-4.

[7] X.J. Chang, M.Q. Zeng, K.L. Liu, L. Fu, Phase engineering of high-entropy alloys, Adv. Mater. 32 (2020) 1907226. https://doi.org/10.1002/adma.201907226.

[8] D.B. Miracle, O.N. Senkov, A critical review of high entropy alloys and related concepts, Acta Mater. 122 (2017) 448-511. https://doi.org/10.1016/j.actamat.2016.08.081.

[9] National Academies of Sciences, Engineering, and Medicine 2019. Frontiers of Materials Research: A Decadal Survey. Washington, DC: The National Academies Press. https://doi.org/10.17226/25244.

[10] K. Holmberg, A. Erdemir, Influence of tribology on global energy consumption, costs and emissions. Friction 5 (2017) 263–284. https://doi.org/10.1007/s40544-017-0183-5.

[11] C. Liu, Z.M. Li, W.J. Lu, Y. Bao, W.Z. Xia, X.X. Wu, H. Zhao, B. Gault, C.L. Liu, Mi. Herbig, A. Fischer, G. Dehm, G. Wu, D. Raabe, Reactive wear protection through strong and deformable oxide nanocomposite surfaces. Nat Commun. 12 (2021) 5518. https://doi.org/10.1038/s41467-021-25778-y.

[12] C. Lee, F. Maresca, R. Feng, Y. Chou, T. Ungar, M. Widom, K. An, J.D. Poplawsky, Y.C. Chou, P.K. Liaw, W.A. Curtin, Strength can be controlled by edge

dislocations in refractory high-entropy alloys, Nat. Commun. 12 (2021) 5474. https://doi.org/10.1038/s41467-021-25807-w.

[13] R. Singh, A. Sharma, P. Singh, G. Balasubramanian, D.D. Johnson, Accelerating computational modeling and design of high-entropy alloys, Nat. Comput. Sci. 1 (2021) 54–61. https://doi.org/10.1038/s43588-020-00006-7.

[14] Chenxi Liu, Chunliang Mao, Lei Cui, Xiaosheng Zhou, Liming Yu, Yongchang Liu, Recent progress in microstructural control and solid-state welding of reduced activation ferritic/martensitic steels, Acta Metall. Sin. 57 (2021) 1521. https://doi.org/10.11900/0412.1961.2021.00348.

[15] Hongwei Wang, Zhufeng He, Nan Jia, Microstructure and mechanical properties of a FeMnCoCr high-entropy alloy with heterogeneous structure, Acta Metall. Sin. 57 (2021) 632. https://doi.org/10.11900/0412.1961.2020.00225.

[16] T. Yang, Y.L. Zhao, W.P. Li, C.Y. Yu, J.H. Luan, D.Y. Lin, F. Fan, Z.B. Jiao, W.H. Liu, X.J. Liu, J.J. Kai, J.C. Huang, C.T. Liu, Ultrahigh-strength and ductile superlattice alloys with nanoscale disordered interfaces, Science 369 (2020) 427-432. https://doi.org/10.1126/science.abb6830.

[17] R.P. Zhang, S.T. Zhao, J. Ding, Y. Chong, T. Jia, C. Ophus, M. Asta, R.O. Ritchie, A.M. Minor, Strength can be controlled by edge dislocations in refractory high-entropy alloys, Nature 581 (2020) 283–287. https://doi.org/10.1038/s41586-020-2275-z.

[18] L.J. Santodonato, Y. Zhang, M. Feygenson, C.M. Parish, M.C. Gao, R.J.K. Weber,

J.C. Neuefeind, Z. Tang, P.K. Liaw, Deviation from high-entropy configurations in the atomic distributions of a multi-principal-element alloy, Nat. Commun. 6 (2015) 5964. https://doi.org/10.1038/ncomms6964.

[19] B. Schönfeld, C.R. Sax, J. Zemp, M. Engelke, P. Boesecke, T. Kresse, T. Boll, T. Al-Kassab, O.E. Peil, A.V. Ruban, Local order in Cr-Fe-Co-Ni: Experiment and electronic structure calculations, Phys. Rev. B, 99 (2019) 014206. https://doi.org/10.1103/PhysRevB.99.014206.

[20] Y. Wu, F. Zhang, X.Y. Yuan, H.L. Huang, X.C. Wen, Y.H. Wang, M.Y. Zhang, H.H. Wu, X.J. Liu, H. Wang, S.H. Jiang, Z.P. Lu, Short-range ordering and its effects on mechanical properties of high-entropy alloys, J Mater. Sci. Technol. 62 (2021) 214-220. https://doi.org/10.1016/j.jmst.2020.06.018.

[21] J.B. Seol, J.W. Bae, J.G. Kim, H. Sung, Z.M. Li, H.W. Lee, S.H. Shim, J.H. Jang, W.S. Ko, S.I. Hong, H.S. Kim, Short-range order strengthening in boron-doped high-entropy alloys for cryogenic applications, Acta Mater. 194 (2020) 366-377. https://doi.org/10.1016/j.actamat.2020.04.052.

[22] C.G. Schön, On short-range order strengthening and its role in high-entropy alloys, Scripta Mater. 196 (2021) 113754. https://doi.org/10.1016/j.scriptamat.2021.113754.

[23] D.L. Bourell, Perspectives on additive manufacturing, Annu. Rev. Mater. Res. 46 (2016) 3.1-3.18. https://doi.org/10.1146/annurev-matsci-070115-031606.

[24] J.J. Lewandowski, M. Seifi, Metal additive manufacturing: a review of

mechanical properties, Annu. Rev. Mater. Res. 46 (2016) 14.1-14.36. https://doi.org/10.1146/annurev-matsci-070115-032024.

[25] D.D. Gu, X.Y. Shi, R. Poprawe, D.L. Bourell, R. Setchi, J.H. Zhu, Material-structure-performance integrated laser-metal additive manufacturing, Science 372 (2021) eabg1487. https://doi.org/10.1126/science.abg1487.

[26] A. Bandyopadhyay, B. Heer, Additive manufacturing of multi-material structures, Mater. Sci. Eng. R 129 (2018) 1-16. https://doi.org/10.1016/j.mser.2018.04.001.

[27] G. Liu, X.F. Zhang, X.L. Chen, Y.H. He, L.Z. Cheng, M.K. Huo, J.N. Yin, F.Q. Hao, S.Y. Chen, P.Y. Wang, S.H. Yi, L. Wan, Z.Y. Mao, Z. Chen, X. Wang, Zhaowenbo Cao, Jian Lu, Additive manufacturing of structural materials, Mater. Sci. Eng. R 145 (2021) 100596. https://doi.org/10.1016/j.mser.2020.100596.

[28] C.J. Han, Q.H. Fang, Y.S. Shi, S.B. Tor, C.K. Chua, K. Zhou, Recent advances on high-entropy alloys for 3D printing, Adv. Mater. 32 (2020) 1903855. https://doi.org/10.1002/adma.201903855.

[29] T. Lehmann, D. Rose, E. Ranjbar, M. Ghasri-Khouzani, M. Tavakoli, H. Henein, T. Wolfe, Large-scale metal additive manufacturing: a holistic review of the state of the art and challenges, Int. Mater. Rev. 67, 410-459 (2021). https://doi.org/10.1080/09506608.2021.1971427.

[30] Y.C. Cai, M.S. Shan, Y. Cui, S.M. Manladan, X. Lv, L.S. Zhu, D. Sun, T. Wang, J. Han, Microstructure and properties of FeCoCrNi high entropy alloy produced by laser melting deposition, J Alloy Compd. 887 (2021) 161323.

https://doi.org/10.1016/j.jallcom.2021.161323.

[31] L.J. Santodonato, P.K. Liaw, R.R. Unocic, H. Bei, J.R. Morris, Predictive multiphase evolution in Al-containing high-entropy alloys, Nat. Commun. 9 (2018) 4520. https://doi.org/10.1038/s41467-018-06757-2.

[32] Y.C. Cai, L.S. Zhu, Y. Cui, K.P. Geng, S.M. Manladan, Z. Luo, J. Han, Strengthening mechanisms in multi-phase $FeCoCrNiAl_{1.0}$ high-entropy alloy cladding layer, Mater. Charact. 159 (2020) 110037. https://doi.org/10.1016/j.matchar.2019.110037.

[33] R. Feng, Y. Rao, C.H. Liu, X. Xie, D.J. Yu, Y. Chen, M. Ghazisaeidi, T. Ungar, H.M. Wang, K. An, P.K. Liaw, Enhancing fatigue life by ductile-transformable multicomponent B2 precipitates in a high-entropy alloy, Nat. Commun. 12 (2021) 3588. https://doi.org/10.1038/s41467-021-23689-6.

[34] Y. Fu, C.D. Dai, H. Luo, D.Y. Li, C.W. Du, X.G. Li, The corrosion behavior and film properties of Al-containing high-entropy alloys in acidic solutions, Appl. Surf. Sci. 560 (2021) 149854. https://doi.org/10.1016/j.apsusc.2021.149854.

[35] Y.C. Cai, L.S. Zhu, Y. Cui, K.P. Geng, S.M. Manladan, Z. Luo, High-temperature oxidation behavior of FeCoCrNiAlx high-entropy alloy coatings, Mater. Res. Express 6 (2019) 126552. https://doi.org/10.1088/2053-1591/ab562d.

[36] X.S. Zhang, Y.B. Tian, S.M. Manladan, Y. Cui, K.P. Geng, Y.C. Cai, J. Han. Effects of Laser Powers on Microstructures and Mechanical Properties of Al0.5FeCoCrNi High-Entropy Alloys Fabricated by Laser Melting Deposition,

Materials 15, 2894 (2022). https://doi.org/10.3390/ma15082894.

[37] Standardization Administration of China. General rule of chemical analysis for hydrogen, oxygen, nitrogen, carbon and sulfur in metallic materials, GB/T 14265 (2017).

[38] Standardization Administration of China. Chemical reagent—General rules for inductively coupled plasma atomic emission spectrometry, GB/T 23942 (2009).

[39] Standardization Administration of China. Particle size analysis—Laser diffraction methods—Part 1: General principles, GB/T 19077 (2008).

[40] Y.C. Cai, X.P. Li, X.B. Xia, Y. Cui, S.M. Manladan, L.S. Zhu, M.D. Shan, D. Sun, T. Wang, X. Lv, J. Han, Fabrication of laminated high entropy alloys using differences in laser melting deposition characteristics of FeCoCrNi and FeCoCrNiAl, J Manuf. Processes 72(2021) 294-308. https://doi.org/10.1016/j.jmapro.2021.10.022.

[41] M. Klinger, More features, more tools, more CrysTBox, J. Appl. Cryst. 50 (2017) 1226-1234. https://doi.org/10.1107/S1600576717006793.

[42] W.F. Hosford, Mechanical Behavior of Materials, Cambridge University Press, New York (2005).

[43] R.W. Hertzberg, Deformation and Fracture Mechanics of Engineering Materials (fourth ed.), John Wiley & Sons, New York (1996).

[44] L. Ratke, P.I. Welch, 13th Biennial Congress – International Deep Drawing Research Group: Efficiency in Sheet Metal Forming, Melbourne, Australia, (1984) 427–435.

[45] J.H. Hollomon, Tensile deformation, Trans. AIME 162 (1945) 268-290.

[46] P. Ludwik, Elemente der Technologischen Mechanik, Springer-Verlag, Berlin (1909).

[47] X.H. Chen, L. Lu, Work hardening of ultrafine-grained copper with nanoscale twins, Scripta Mater. 57 (2007) 133-136. https://doi.org/10.1016/j.scriptamat.2007.03.029.

[48] N. Afrin, D.L. Chen, X. Cao, M. Jahazi, Strain hardening behavior of a friction stir welded magnesium alloy, Scripta Mater. 57 (2007) 1004-1007. https://doi.org/10.1016/j.scriptamat.2007.08.001.

[49] Y.H. Rong, Characterization of microstructures by analytical electron microscopy (AEM), High Education Press, Beijing (2012).

[50] T. Xiong, W.F. Yang, S.J. Zheng, Z.R. Liu, Y.P. Lu, R.F. Zhang, Y.T. Zhou, X.H. Shao, B. Zhang, J. Wang, F.X. Yin, P.K. Liaw, X.L. Ma, Faceted Kurdjumov-Sachs interface-induced slip continuity in the eutectic high-entropy alloy, $AlCoCrFeNi_{2.1}$, J Mater. Sci. Technol. 65 (2021) 216-227. https://doi.org/10.1016/j.jmst.2020.04.073.

[51] W.H. Liu, Y. Tong, S.W. Chen, W.W. Xu, H.H. Wu, Y.L. Zhao, T. Yang, X.L. Wang, X.J. Liu, J.J. Kai, C.T. Liu, Unveiling the electronic origin for pressure-induced phase transitions in high-entropy alloys, Matter 2 (2020) 751-763. https://doi.org/10.1016/j.matt.2019.12.023.

[52] Chen S, Aitken Z H, Pattamatta S, Wu Z X, et al. Simultaneously enhancing the ultimate strength and ductility of high-entropy alloys via short-range ordering, Nat.

Commun. 12, 4953 (2021). https://doi.org/10.1038/s41467-021-25264-5.

[53] S. Chen, Z. H. Aitken, S. Pattamatta, Z.X. Wu, Z.G. Yu, D. J. Srolovitz, P.K. Liaw, Y.W. Zhang, Repulsion leads to coupled dislocation motion and extended work hardening in bcc metals, Nat. Commun. 11 (2020) 5098. https://doi.org/10.1038/s41467-020-18774-1.

[54] S. Takebayashi, T. Kunieda, N. Yoshinaga, K. Ushioda, S. Ogata, Comparison of the dislocation density in martensitic steels evaluated by some X-ray diffraction methods, ISIJ Int. 50 (2010) 875-882. https://doi.org/10.2355/isijinternational.50.875.

[55] G.K. Williamson, W.H. Hall, W H. X-ray line broadening from filed aluminium and wolfram, Acta Metall., 1 (1953) 22-31. https://doi.org/10.1016/0001-6160(53)90006-6.

[56] R.J. Shi, Y. Ma, Z.D. Wang, L. Gao, X.S. Yang, L.J. Qiao, X.L. Pang, Atomic-scale investigation of deep hydrogen trapping in NbC/α-Fe semi-coherent interfaces, Acta Mater. 200 (2020) 686-698. https://doi.org/10.1016/j.actamat.2020.09.031.

[57] X.D. Wang, Z. Zhang, Z.B. Wang, X.C. Ren, Excellent tensile property and its mechanism in Al0.3CoCrFeNi high-entropy alloy via thermo-mechanical treatment, J Alloy Compd. 897 (2022) 163218. https://doi.org/10.1016/j.jallcom.2021.163218.

[58] T. Maity, K.G. Prashanth, Ö. Balcı, J.T. Kim, T. Schöberl, Z. Wang, J. Eckert, Influence of severe straining and strain rate on the evolution of dislocation structures during micro-/nanoindentation in high entropy lamellar eutectics, Int. J Plasticity 109

(2018) 121-136. https://doi.org/10.1016/j.ijplas.2018.05.012.

[59] S.J. Sun, Y.Z. Tian, H.R. Lin, H.J. Yang, X.G. Dong, Y.H. Wang, Z.F. Zhang, Transition of twinning behavior in CoCrFeMnNi high entropy alloy with grain refinement, Mater. Sci. Eng. A 712 (2018) 603–607. https://doi.org/10.1016/j.msea.2017.12.022.

[60] J. Zhou, H.C. Liao, H. Chen, A.J. Huang, Effects of hot-forging and subsequent annealing on microstructure and mechanical behaviors of Fe35Ni35Cr20Mn10 high-entropy alloy, Mater. Charact. 178 (2021) 111251. https://doi.org/10.1016/j.matchar.2021.111251.

[61] B. Gwalani, S. Gorsse, D. Choudhuri, Y.F. Zheng, R.S. Mishra, R. Banerjee, Tensile yield strength of a single bulk Al0.3CoCrFeNi high entropy alloy can be tuned from 160 MPa to 1800 MPa, Scr. Mater. 162 (2019) 18–23. https://doi.org/10.1016/j.scriptamat.2018.10.023.

[62] T. Gladman T, Precipitation hardening in metals, Mater. Sci. Tech. 15 (1999) 30-36. https://doi.org/10.1179/026708399773002782.

[63] M.X. Yang, Y. Pan, F.P. Yuan, Y.T. Zhu, X.L. Wu, Back stress strengthening and strain hardening in gradient structure. Mater. Res. Lett. 4 (2016) 145–151. https://doi.org/10.1080/21663831.2016.1153004.

[64] M.X. Yang, D.S. Yan, F.P. Yuan, P. Jiang, E. Ma, X.L. Wu, Dynamically reinforced heterogeneous grain structure prolongs ductility in a medium-entropy alloy with gigapascal yield strength. Proc. Natl. Acad. Sci. USA 115 (2018) 7224–7229.

https://doi.org/10.1073/pnas.1807817115.

Figure caption:

Fig. 1 (a) Schematic diagram of LMD system and processing route; (b) morphology of cross section (Y-Z plane); (c) schematic diagram of sampling.

Fig. 2 Mechanical properties of LMD-ed $FeCoCrNiAl_{0.5}$: (a) true stress-strain curves and (b) fitted work hardening exponents (linear function images); microstructure: (c) SEM image of tensile fracture and (d) EBSD phase distribution image.

Fig. 3 (a) TEM image of LMD-ed FeCoCrNiaL0.5 HEA; (b-e) SAED patterns of zone 'A' in (a); (f-i) SAED patterns of zone 'B' in (a).

Fig. 4 (a) Distribution of GND density in FCC phase zones; (b) distribution of GND density in B2 phase zones; (c-f) TEM image showing dislocations distributions and phase boundaries: (d) is the local magnification of (c), (f) is the local magnification of (e).

Fig. 5 (a) HR-TEM image with FFT pattern of FCC-B2 phase boundary; (b) FFT pattern of FCC-zone 'A' in (a); (c) IFFT lattice fringe of FCC-zone 'A' based on the marked spots in (b); (d) FFT patterns of B2-zone 'B' in (a); (e) IFFT lattice fringe of B2-zone 'B' based on the marked spots in (d); IFFT lattice fringe of boundary-zone 'C' in (a).

Fig. 6 (a) HR-TEM image of FCC-B2 phase boundary with FFT pattern; (b) FFT pattern of B2-zone in (a); (c) FFT pattern of FCC-zone in (a).

Fig. 7 (a) HR-TEM image of FCC-B2 phase boundary with FFT pattern of B2-zone 'B'; (b) IFFT lattice fringe of FCC-zone 'A' in (a); (c) IFFT lattice fringe of B2-zone

‘B’ in (a).

Fig. 8 (a) TEM image of slender B2-zone and phase boundary; (b) TEM of dislocation tangle at grain boundary.

Fig. 9 XRD pattern of LMD-ed $FeCoCrNiAl_{0.5}$ HEA.

Fig. 10 Simulated diffraction pattern of phase boundary at the zone axis $[001]_{B2}//[0\text{-}11]_{FCC}$.

Fig. 11 Atomic diagram at phase boundary.

Fig. 12 Diagram of strain-hardening mechanism of LMD-ed $FeCoCrNiAl_{0.5}$ HEA: (a) before stress; (b) under stress.

Tables:

Table 1 Accurate chemical composition of $FeCoCrNiAl_{0.5}$ powders.

Table 2 Mechanical properties of LMD-ed $FeCoCrNiAl_{0.5}$ in this study.

Table 3 EDS results of zone ‘A’ and zone ‘B’ in Fig. 3a.

Declaration of interests

☒ The authors declare that they have no known competing financial interests or personal relationships that could have appeared to influence the work reported in this paper.

☐The authors declare the following financial interests/personal relationships which may be considered as potential competing interests:

Highlights

1. The LMD-ed FeCoCrNiAl0.5 HEA displayed a good strain hardening behaviour.

2. The boundary between the disordered FCC and ordered B2 phases blocks the movement of dislocations under stress.

3. Dislocation pile-up and tangle nearby the phase boundary improve the strain hardening property.



https://dspace.org/

Strain hardening and strengthening mechanism of laser melting deposition (LMD) additively manufactured FeCoCrNiAl0.5 high-entropy alloy

Zhu, Lisong; Geng, Keping; Wang, Jun; Sun, Da; Shan, Mengdie ...

2022-10-05
Elsevier
https://doi.org/10.1016/j.matchar.2022.112365
Zhu L, Geng K, Wang J, et al., (2022) Strain hardening and strengthening mechanism of laser melting deposition (LMD) additively manufactured FeCoCrNiAl0.5 high-entropy alloy, Materials Characterization, Volume 194, December 2022, Article number 112365

Downloaded from a DSpace repository. https://dspace.org/